Ionics (2022) 28:4967–4976
https://doi.org/10.1007/s11581-022-04755-5

ORIGINAL PAPER

Facile synthesis of yolk-shell CoS_2@FeS_2@NC hollow microspheres for advanced lithium-ion batteries anode materials

Dongxuan Liu[1] · **Weixing Min**[1] · **Ping Chen**[1] · **Dongwei Xu**[1] · **Xinrong Cao**[1] · **Guanzhen Chen**[1] · **Ruiqi Wang**[1]

Received: 12 May 2022 / Revised: 20 August 2022 / Accepted: 9 September 2022 / Published online: 17 September 2022

Abstract

Transition metal chalcogenides (TMCs) are considered to be promising as anode materials for lithium-ion batteries (LIBs) due to their unique physical and chemical properties and high theoretical specific capacity. Nevertheless, the poor rate performance and fast capacity decay seriously affect its practical application in LIBs. In the present study, porous yolk-shell CoS_2@FeS_2@NC hollow microspheres have been successfully prepared through a simple step-by-step strategy. In addition to shortening the transport length of lithium ions, this unique structure can also successfully alleviate the volume change during charging/discharging. Importantly, the coating of the nitrogen-doped carbon (NC) layer effectively enhances the electrical conductivity of the material and prevents exfoliation of metal particles. The yolk-shell CoS_2@FeS_2@NC hollow microspheres show high specific capacity (1162.6 mAh g^{-1}) and excellent cycle stability (614 mAh g^{-1} at 1 A g^{-1} after 100 cycles) when used as anode material for LIBs. These fascinating electrochemical performances strongly demonstrate that the as-obtained yolk-shell CoS_2@FeS_2@NC hollow microspheres can be highly applicable in the field of high-performance LIBs electrode materials.

Keywords Transition metal chalcogenides · Lithium-ion batteries · Carbon · Electrochemical performance · Anode materials

Introduction

With the rapid development of portable electronic devices and electric vehicle industries, LIBs [1–4], lithium-sulfur batteries [5–8], and fuel cells are regarded as energy storage devices with great potential for development. Among them, LIBs have been widely used in various industries because of their long life span, high energy density, light weight, and environmental protection [9]. Graphite, employed as the anode material of current LIBs, own good stability, but its inherent low specific capacity also seriously restricts the development of high-energy–density LIBs. In order to meet the growing application demands, many researchers have invested a lot of time in developing high-performance anode materials, hoping to replace traditional graphite and further improve the electrochemical performance of LIBs [10, 11].

TMCs, as the promising candidate, such as FeS_2, CoS_2, MoS_2, ReS_2, NiS_2, and NiS, make full use of all oxidation states of transition metals and result in a rich reversible redox reaction, which makes them own high theoretical capacity and has attracted extensive attention [12–19]. Nonetheless, the inherently low electrical conductivity, the structural pulverization, and the large volume change of TMCs lead to rapid capacity decay during charge and discharge, which significantly restricts the cycling stability of TMCs in LIBs [20–22]. To solve the above problems, lots of strategies to enhance the performance of lithium storage have been proposed. One effective approach is to design nanostructures with a high specific surface area, thereby shortening the transfer length of Li^+ intercalation [23–29]. For example, Hao et al. reported that a material composed of MnS nanocrystals only provided a specific capacity of 287 mA h g^{-1} at 100 mA g^{-1} [30]. The problem of capacity fading caused by its pulverization, inherent low electronic conductivity, and aggregation of metal particles during cycling cannot be solved by mere nanostructure engineering. So another approach of integrating nanostructured TMCs with carbon-based materials has been proposed to

✉ Ping Chen
chenping_898@126.com

[1] State Key Laboratory of Fine Chemicals, School of Chemical Engineering, Dalian University of Technology, Dalian 116024, China

solve the aforementioned issues [31–36]. In this method, in addition to the advantages of TMCs, the introduced carbon component provides a stable conductive framework, which can enhance the conductivity of the material and well alleviate the volume change during charging and discharging, thereby improving the electrochemical performance.

Herein, the yolk-shell CoS_2@FeS_2@NC hollow microspheres are successfully synthesized by a multistep process containing the fabrication of solid Co-glycerate (Co-G) precursor, the growth of Fe-glycerate (Fe-G) nanosheets, polydopamine (PDA) coating, and subsequent sulfurization process. The CoS_2@FeS_2@NC hybrid materials have the following advantages: (1) the yolk-shell structure can effectively buffer the volume change, provide more active centers, and greatly shorten the transfer paths of lithium-ions since the large specific surface area plays an important role in facilitating ion transportation. (2) Compared to single metal sulfides, the integration of CoS_2 with FeS_2 into nanostructure not only preserves advantages of individual components, but also effectively exploits the synergistic effect between different metal sulfides, which can achieve excellent electrochemical performance [37–39]. (3) The coating of the NC layer not merely effectively enhances the electrical conductivity and structural stability of the material, but also inhibits the exfoliation and aggregation of FeS_2 nanoparticles during the lithium insertion/extraction process. Therefore, after 100 cycles, the specific capacity of the CoS_2@FeS_2@NC composites can be maintained at 614 mA h g^{-1} at 1 A g^{-1}, showing high specific capacity and outstanding cycling stability.

Experimental section

Preparation of Co-G microspheres

The synthesis process of Co-G microspheres is referred to the previous literature [40]. In a typical synthesis, $Co(NO_3)_2 \cdot 6H_2O$ (0.546 g) was added into a mixed isopropanol and glycerol solution (240 mL) with an isopropanol/glycerol volume ration of 5:1. After rapid stirring for a few minutes, the solution turned clear pink and was transferred into a 300 mL Teflon-lined autoclave, followed by heating at 180 ℃ for 6 h. After that, the pink products were centrifugally separated and rinsed with ethanol and dried at 70 ℃ for 10 h, denoted as Co-G.

Preparation of yolk-shell Co-G@Fe-G hollow microspheres

Typically, $Fe(NO_3)_3 \cdot 9H_2O$ (50 mg) was homogeneously dispersed in the solution containing glycerol (10 mL) and isopropanol (70 mL) by ultrasonication. Then, as-prepared Co-G (35 mg) was added into the solution and sonicated for 10 min. Finally, the resulting mixture was poured into 100 mL Teflon-lined autoclave and reacted at 190 ℃ for 10 h. The dark brown sediments were obtained through centrifugation, washed three times with ethanol and deionized, and dried at 70 ℃ overnight, denoted as Co-G@Fe-G.

Preparation of yolk-shell CoS_2@FeS_2@NC hollow microspheres

To coat the NC layer, the prepared Co-G@Fe-G microspheres (50 mg) were uniformly dispersed into 100 mL Tris-buffer solution (10 M) and sonicated for 30 min. Then, dopamine hydrochloride (25 mg) was added into the suspension, which was stirred at 25 ℃ for 6 h. The suspension was suction filtered, washed with deionized water, and dried at 70 ℃ overnight to obtain black products. Finally, as-prepared black products (0.1 g) and sublimed sulfur (0.3 g) were thoroughly ground for 5 min. In nitrogen atmosphere, the mixtures were placed in a small quartz boat and heated at 350 ℃ for 4 h with a ramp rate of 2 ℃·min^{-1}. After cooling, the final products were obtained, denoted as CoS_2@FeS_2@NC. For comparison, yolk-shell CoS_2@FeS_2 microspheres were synthesized with the same procedure except for the absence of the PDA coating process.

Results and discussion

The fabrication procedure of yolk-shell CoS_2@FeS_2@NC hollow microspheres is vividly depicted in Fig. 1. Firstly, Co-G microspheres precursor samples are synthesized and Fe-G nanosheets are sequentially grown on the surface of Co-G microspheres via the solvothermal process. The phenomenon of uniform growth of Fe-G nanosheets on the surface of the Co-G microspheres can be explained by the previously reported heterogeneous nucleation and self-templated evolution processes. [40–42]. In the coexistence of isopropanol (IPA) and glycerol, iron ions are firstly coordinated with IPA molecules and then uniformly grown on the prepared Co-G microspheres. Under the current synthesis conditions, with the progress of the reaction, the Fe-IPA (forms of coordination binding of iron ions with isopropanol molecules) layers gradually transform into Fe-G nanosheets. While the Fe-G nanosheets are growing, Co-G begins to decompose under the influence of Fe^{3+}. Due to the different decomposition speeds of the inner and outer surfaces, the yolk-shell structure is finally formed. Afterward, a layer of PDA is coated on the yolk-shell Co-G@Fe-G hollow microspheres to obtain Co-G@Fe-G@PDA hollow microspheres. Finally, the as-prepared Co-G@Fe-G@PDA composites are transformed into CoS_2@FeS_2@NC by in situ carbonization and sulfuration.

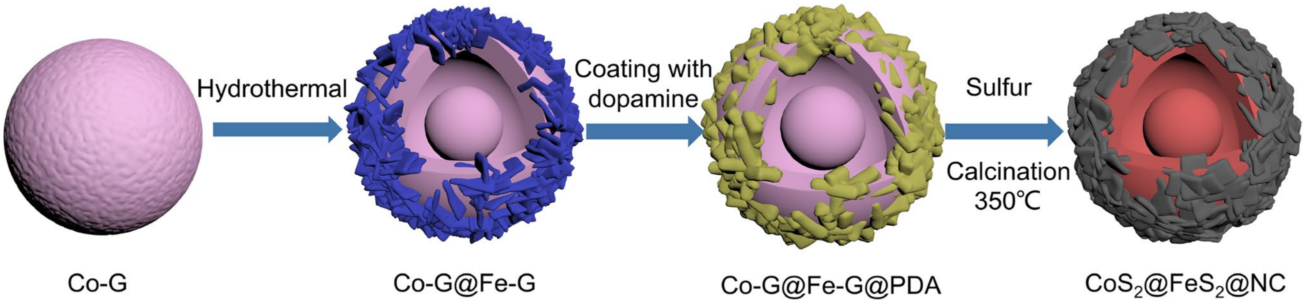

Fig. 1 Fabrication process of yolk-shell CoS_2@FeS_2@NC hollow microspheres

Typical scanning electron microscopy (SEM) and transmission electron microscopy (TEM) well demonstrate the morphologies and detailed structures of CoS_2@FeS_2@NC hollow microspheres. The as-obtained Co-G microspheres demonstrate a smooth surface and spherical morphologies with a rather uniform size of about 600 nm (Fig. 2a). The uniform Fe-G nanosheets are synthesized by the solvothermal process on the surface of Co-G nanospheres, which can be well proved by the SEM image (Fig. 2b and Fig. S1). As can be seen from Fig. 2c, the thickness of the nanosheets on the surface of the microspheres increases significantly, indicating that Co-G@Fe-G microspheres are successfully coated with PDA. Additionally, we can clearly observe the yolk-shell structure from one of the broken microspheres (Fig. S1 and Fig. 2c). The TEM images are adopted to investigate the interior structure of CoS_2@FeS_2@NC microspheres, which further confirms the yolk-shell and hollow structure (Fig. 3a, b). As shown in Fig. 2d, after high-temperature sulfuration, the diameter of the microspheres reduces from 850 to 750 nm before calcination. The reason for the shrinkage is that the nanosheets are partially cracked into nanoparticles at this temperature, and the external polydopamine is transformed into nitrogen-doped carbon. It is clearly seen from the TEM image that the thickness of the carbon layer is approximately 35 nm (Fig. 3c). Furthermore, it is evident from the high-resolution TEM (HRTEM) image that the lattice spacings of 0.19 nm and 0.27 nm correspond to the (220) plane of the CoS_2 and the (200) plane of the FeS_2, respectively, which agrees with XRD spectra (Fig. 3d). The high-angle annular dark-field scanning transmission electron microscopy (HAADF-STEM) image and X-ray mapping images show that Fe, Co, S, C, and N elements are homogeneously distributed throughout the microsphere (Fig. 3e). Table S1 further demonstrates the presence and content of above elements. For comparison, the morphology of CoS_2@FeS_2 is also illustrated by the SEM image in Fig. S2.

Fig. 2 **a** SEM images of Co-G, **b** Co-G@Fe-G, **c** Co-G@Fe-G@PDA, **d** CoS_2@FeS_2@NC

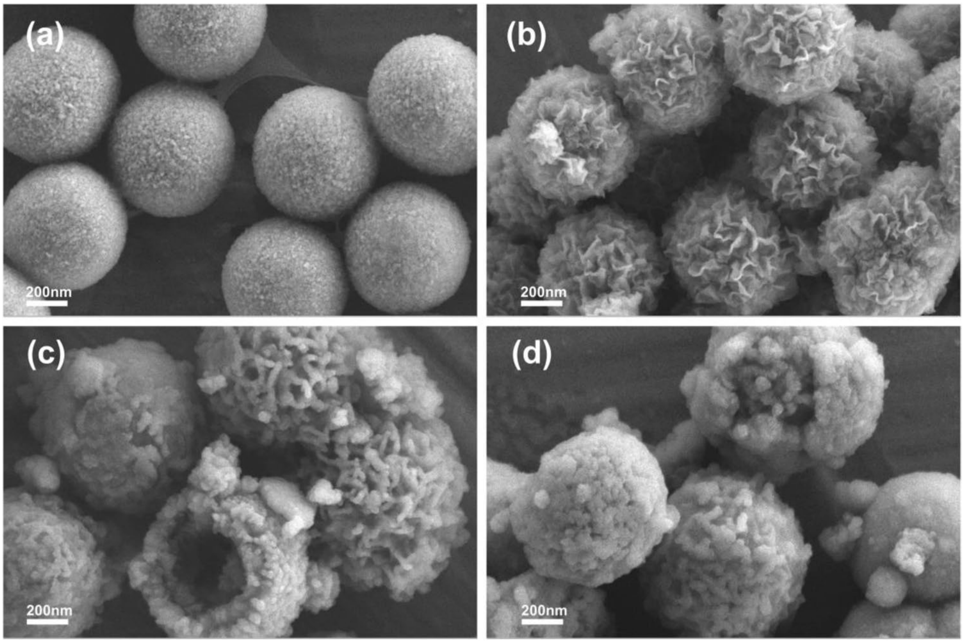

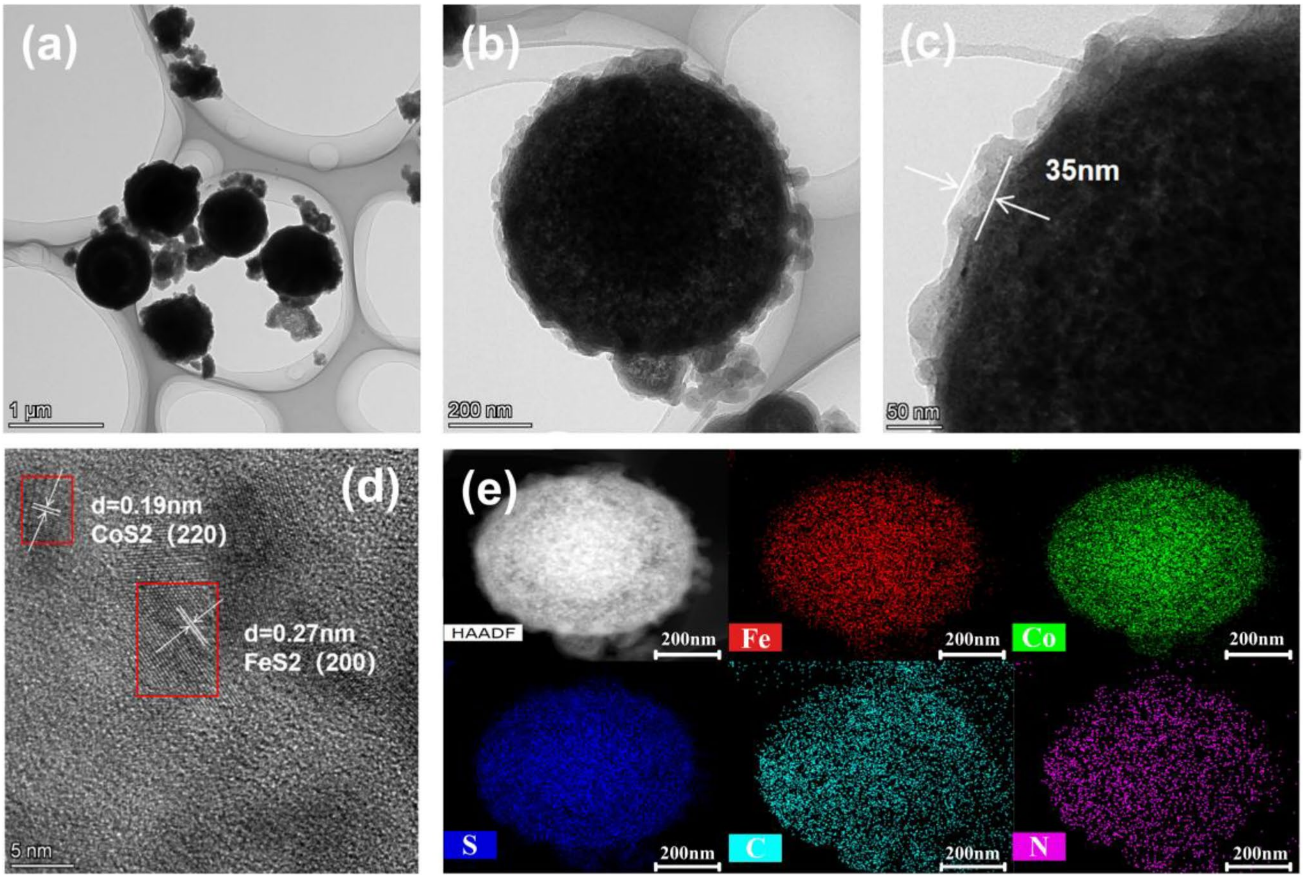

Fig. 3 **a–c** TEM images of $CoS_2@FeS_2@NC$ with different magnifications, **d** HRTEM image of $CoS_2@FeS_2@NC$, and **e** corresponding EDX elemental mapping images of $CoS_2@FeS_2@NC$

Figure 4a exhibits the X-ray diffraction (XRD) pattern of $CoS_2@FeS_2@NC$ composites. The characteristic peaks at 28.7°, 32.5°, 36.7°, 46.8°, 50.9°, and 64.4° can be indexed to the (111), (200), (210), (220), (221), and (321) planes of FeS_2 (JCPDS#42–1340), respectively [43, 44]. The peaks located at 32.5°, 40.3°, 46.8°, 55.4°, and 60.6° perfectly correspond to the (200), (211), (220), (311), and (230) planes of CoS_2 (JCPDS#41–1471), respectively [44, 45]. Simultaneously, there is no obvious C peak in the XRD results, indicating the carbon in the material mainly exists in the form of amorphous carbon. From the XRD pattern, the $CoS_2@FeS_2@NC$ composites exhibit excellent crystallinity.

Figure 4b depicts the Raman spectrum of $CoS_2@FeS_2@NC$, in which two prominent peaks located around 1398 cm^{-1} and 1550 cm^{-1} correspond to the D band and G band, respectively. The D band is mainly related to Raman

Fig. 4 **a** XRD patterns and **b** Raman spectra of $CoS_2@FeS_2@NC$

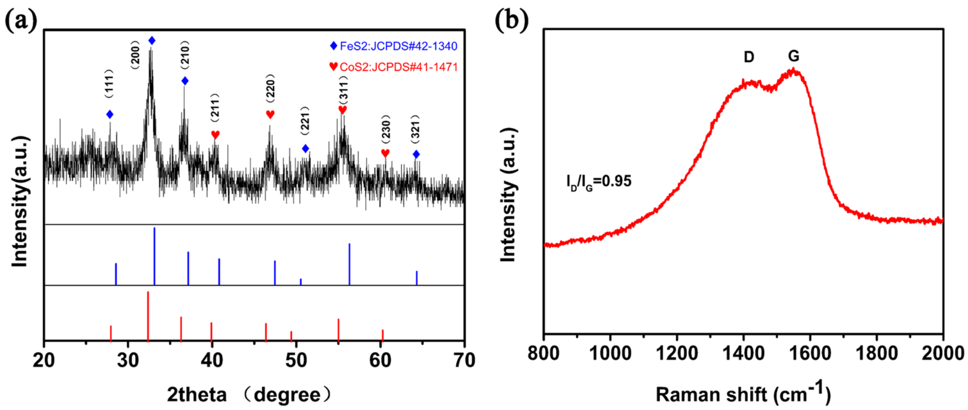

scattering introduced by internal structure defects or disorder, while the G band is chiefly due to the stretching vibration of sp2 hybrid carbon atoms [46–48]. The calculated value of I_D/I_G is relatively high 0.95. Combined with XRD analysis, it indicates that there are abundant topological defects and disorder in NC, which is favorable for lithium storage [49]. The BET analysis showed that the specific surface area of the yolk-shell CoS_2@FeS_2@NC hollow microspheres is 14.94 m^2 g^{-1} and the pore size is mainly distributed around 2.77 nm and 15–85 nm (Fig. S3), which greatly shortens the diffusion length of Li^+ and enhances the electrochemical performance of LIBs.

The surface chemical valence states of the CoS_2@FeS_2@NC nanospheres are further verified by X-ray photoelectron spectroscopy (XPS) analyses. Fig. 5a indicates that the samples are composed of Fe, Co, S, C and N five elements. Furthermore, the spectra of Fe 2p (Fig. 5b) and Co 2p (Fig. 5c) are fitted with two spin–orbit doublets and shakeup satellites (denoted as "Sat."). From the Fe 2p spectrum (Fig. 5b), it can be seen that two distinct peaks located at 713.2 and 726.6 eV correspond to the Fe $2p_{3/2}$ and Fe $2p_{1/2}$ binding energies, respectively [44, 50]. Similarly, two typical peaks at 781.8 and 801.0 eV can be indexed to Co^{2+} $2p_{3/2}$ and Co^{2+} $2p_{1/2}$, which indicates the existence of Co^{2+} [44, 51]. There are three fitted peaks in the S 2p spectrum (Fig. 5d), of which the two peaks at 163.6 and 164.6 eV are assigned to $2p_{3/2}$ and $2p_{1/2}$ of the S element in the composites, demonstrating the existence of S–S bonds in the CoS_2@FeS_2@NC. Additionally, the peak located at 168.6 eV is attributed to the S–O bond generated by the surface oxidation of CoS_2@FeS_2@NC composites [15, 51]. As can be seen from Fig. 5e, the C 1 s spectrum is divided into three peaks at 284.6 eV, 285.9 eV, and 288.4 eV, indicating the presence of C–C, C-N and C-O, respectively [52]. The N 1 s XPS spectrum is curve-fitted with three characteristic peaks at 398.8 eV, 400.0 eV, and 400.9 eV, corresponding to pyridinic N, pyrrolic N, and graphitic N, respectively [43, 53].

The electrochemical properties of the CoS_2@FeS_2@NC composites is evaluated. Fig. 6a exhibits typical CV curves of CoS_2@FeS_2@NC for the first five cycles in the 0.01–3.0 V (vs. Li/Li^+) voltage window. During the first cathodic scan, the peaks at 0.51 and 0.68 V can be attributed to the formation of a solid electrolyte interface (SEI) layer on the electrode surface [54–57]. The two reduction peaks near 1.18 and 1.29 V are caused by the insertion of Li^+ into FeS_2 (Eq. (1) and Eq. (2)) [58]. In addition, the reduction peaks appearing at 1.50 and 1.93 V are due to the insertion of Li^+ into CoS_2 (Eq. (3) and Eq. (4)) [54]. The first anodic curve revels four oxidation peaks at 1.91, 2.05, 2.30, and 2.48 V, respectively, of which the oxidation peaks located at 2.05 and 2.30 V are related to the Li^+ extraction of CoS_2 (Eq. (5) and Eq. (6)). The other two oxidation peaks at 1.91 and 2.48 V correspond to the formation of Li_2FeS_2 (Eq. (7)) and FeS_y/S (Eq. (8) and Eq. (9)), respectively [55]. The two reduction peaks of CoS_2 move from their previous positions to 1.26 and 1.82 V, respectively, during the subsequent

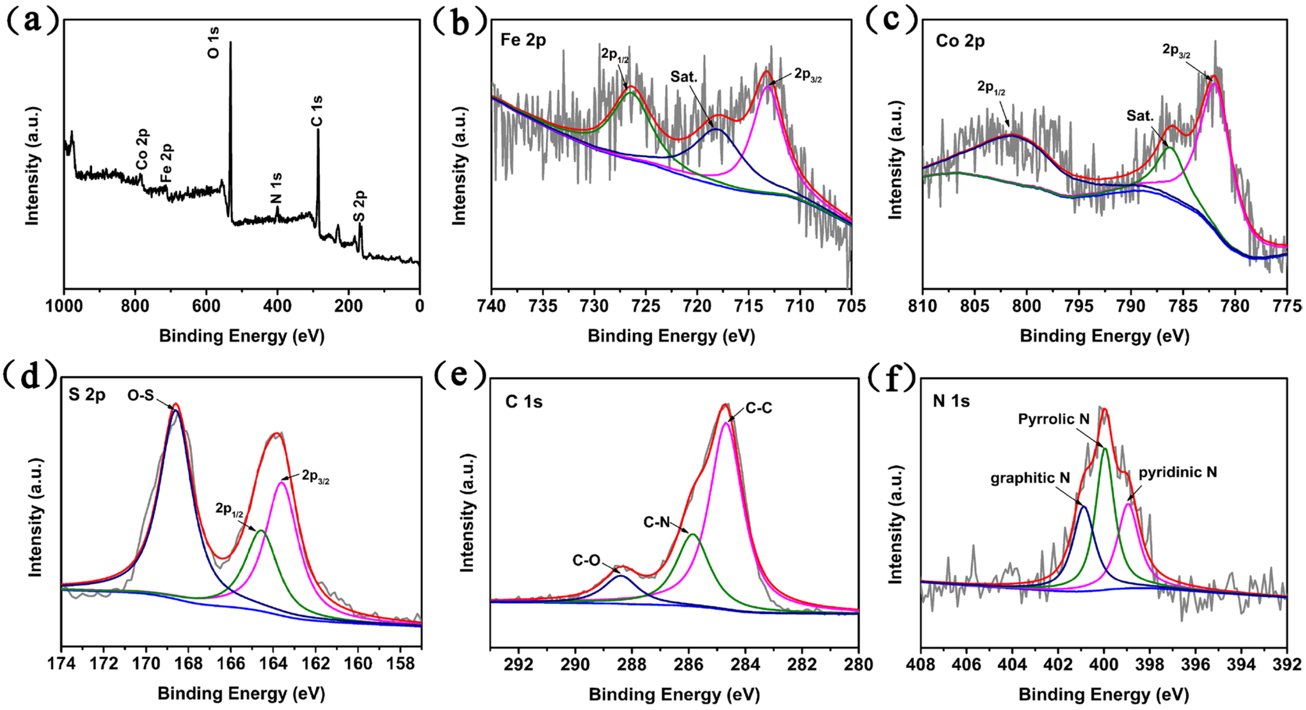

Fig. 5 **a** XPS survey scan, **b** Fe 2p, **c** Co 2p, **d** S 2p, **e** C 1 s, and (**f**) N 1 s high-resolution spectrum for CoS_2@FeS_2@NC

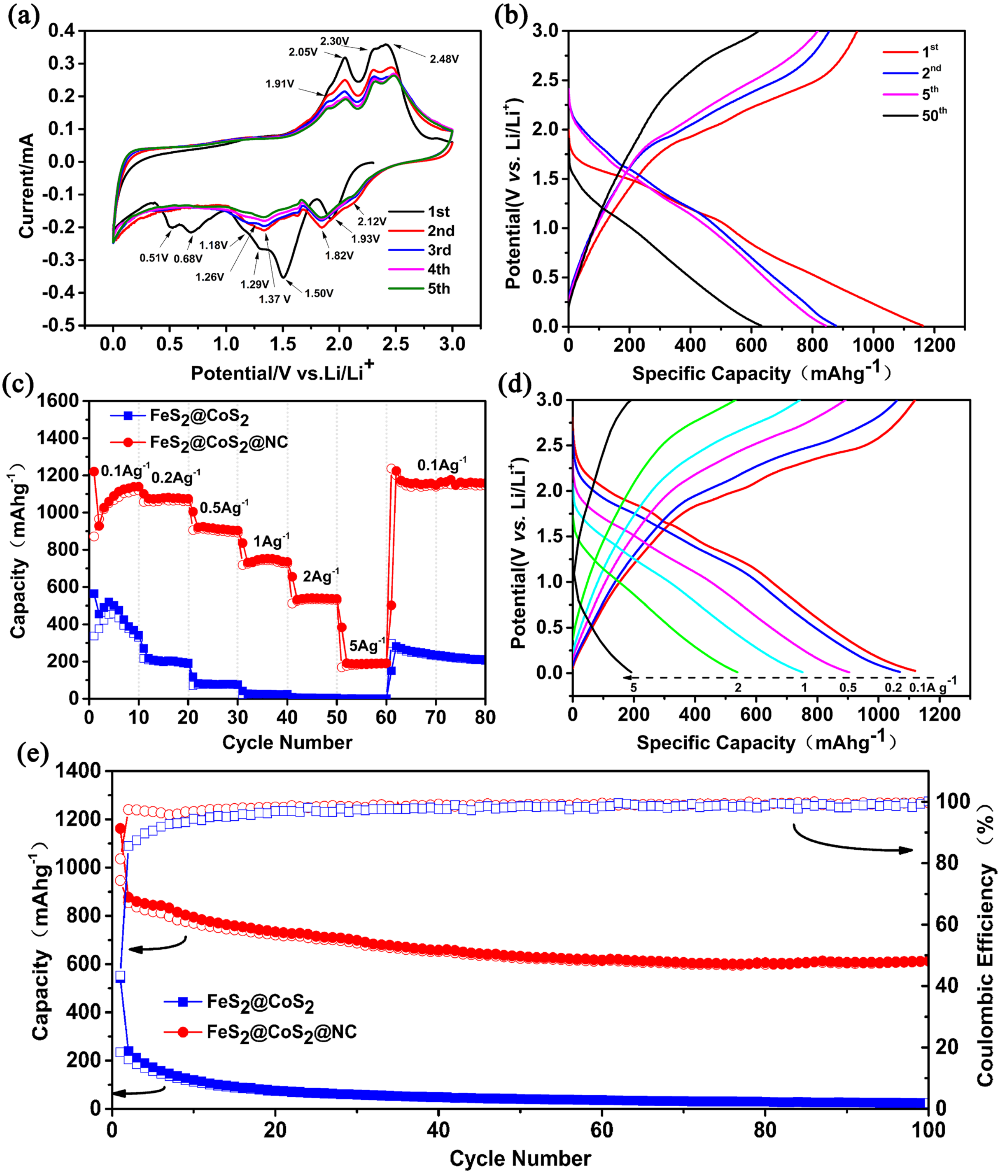

Fig. 6 Electrochemical performance of yolk-shell CoS_2@FeS_2@NC hollow microspheres. **a** CV curves at a scan rate of 0.1 mV s^{-1}. **b** The discharge–charge voltage profiles at 1 A g^{-1}. **c** Rate performance and **d** the corresponding discharge–charge curves at different current densities. **e** Cycling performance and coulombic efficiency at 1 A g^{-1}

cycling. Moreover, the reduction peak at 2.12 V is assigned to the formation of Li_2FeS_2 (Eq. (10)), while the peak at 1.37 V is ascribed to the formation of Fe/Li_2S (Eq. (11)) [43, 58]. Except for the first circle, the remaining CV curves basically overlap, demonstrating the excellent cycling stability and reversibility of the CoS_2@FeS_2@NC electrode.

$$FeS_2 + 2Li^+ + 2e^- \rightarrow Li_2FeS_2 \tag{1}$$

$$Li_2FeS_2 + 2Li^+ + 2e^- \rightarrow Fe + 2Li_2S \tag{2}$$

$$CoS_2 + xLi^+ + xe^- \rightarrow Li_xCoS_2 \tag{3}$$

$$Li_xCoS_2 + (4 - x)Li^+ + (4 - x)e^- \rightarrow Co + 2Li_2S \tag{4}$$

$$Co + 2Li_2S \rightarrow Li_xCoS_2 + (4 - x)Li^+ + (4 - x)e^- \tag{5}$$

$$Li_xCoS_2 \rightarrow CoS_2 + xLi^+ + xe^- \tag{6}$$

$$Fe + 2Li_2S \rightarrow Li_2FeS_2 + 2Li^+ + 2e^- \tag{7}$$

$$Li_2FeS_2 \rightarrow Li_{2-x}FeS_2 + xLi^+ + xe^- \tag{8}$$

$$Li_{2-x}FeS_2 \rightarrow FeS_y + (2 - y)S + (2 - x)Li^+ + (2 - x)e^- \tag{9}$$

$$FeS_y + (2 - y)S + 2Li^+ + 2e^- \rightarrow Li_2FeS_2 \tag{10}$$

$$Li_2FeS_2 + 2Li^+ + 2e^- \rightarrow Fe + 2Li_2S \tag{11}$$

Figure 6b shows the typical discharge/charge voltage profiles of the CoS_2@FeS_2@NC electrode at a current density of 1 A g^{-1} in a voltage window of 0.01–3.0 V (vs. Li/Li^+). The discharge and charge capacities in the first cycle are 1162.6 $mAhg^{-1}$ and 946.6 mAh g^{-1}, corresponding to an initial columbic efficiency (CE) of 81.4%. The low CE of the battery is primarily due to the reductive decomposition of the electrolyte and the formation of the SEI layer during the charge–discharge process [59–61]. What is more, the reaction between lithium ions and the remaining functional groups of the PDA-derived carbon also affects CE [51]. During the second cycle, the discharge capacity reduces to 877.1 $mAhg^{-1}$ and the corresponding charge capacity is 854.7 $mAhg^{-1}$, resulting in a high CE of 97.5%. In the subsequent cycles, the CE of 96.8% and 98.7% are observed at the 5th and 50th cycle, respectively, which manifests excellent reversibility of the charge/discharge process.

To highlight the electrochemical performance of CoS_2@FeS_2@NC, the rate performance of CoS_2@FeS_2 is also evaluated. Fig. 6c shows the rate performance of the electrodes made of yolk-shell CoS_2@FeS_2@NC hollow microspheres and yolk-shell CoS_2@FeS_2 hollow microspheres cycled under different current densities. The results show that CoS_2@FeS_2@NC battery own higher capacity and better stability than CoS_2@FeS_2 battery at various current densities. When the current density gradually increases from 0.1 to 0.2, 0.5, 1.0, 2.0, and 5 A g^{-1}, the corresponding specific capacities decrease from 1097 to 1076, 922, 752, 549, and 209 $mAhg^{-1}$, respectively. In addition, when the current density is restored to 0.1 A g^{-1}, the specific capacity can quickly return to 1130 $mAhg^{-1}$, demonstrating that the CoS_2@FeS_2@NC electrode has excellent reversibility for lithium storage. It can be seen that at the current density of 0.1 A g^{-1}, the capacity of the last twenty cycles is higher than that of the first ten cycles. The main reason for this phenomenon is that the electrolyte penetrates into the inner cavity to activate the active material [14, 62–64]. The discharge–charge voltage curves at different current densities further confirm the excellent rate capability of the CoS_2@FeS_2@NC electrode (Fig. 6e).

Moreover, the CoS_2@FeS_2@NC electrode also shows excellent cycling stability. Fig. 6e exhibits the cycling performance over 100 cycles at a current density of 1 A g^{-1}. The specific capacity of the CoS_2@FeS_2 electrode rapidly decays to 76 mAh g^{-1} along with a CE of about 97% after only 20 cycles. In contrast, the CoS_2@FeS_2@NC composite can still stabilize at a high specific capacity of 614 mAh g^{-1} without significant decrease after 100 cycles. The initial CE of 81% gradually increases and stabilizes at more than 98% after 16 cycles, further proving the outstanding cycling stability of CoS_2@FeS_2@NC. The performance improvement is due to the introduction of NC layer. On the one hand, the NC layer can prevent structural exfoliation of FeS_2 nanoparticles and inhibit the dissolution of polysulfides. On the other hand, the NC layer coated on the surface of FeS_2 nanoparticles can improve the conductivity and electrochemical activity.

Through electrochemical impedance spectra (EIS), we can further study the reason why the CoS_2@FeS_2@NC composites have better electrochemical performance than CoS_2@FeS_2 for LIBs. The Nyquist plots (Fig. S4) of CoS_2@FeS_2@NC and CoS_2@FeS_2 are composed of semicircles and oblique straight lines. The semicircle in the high-frequency region and the oblique straight lines in the low-frequency region correspond to the charge transfer resistance between electrolyte and electrode material (R_{ct}) and Li^+ diffusion impedance, respectively [31, 65, 66]. Obviously, in high-frequency range, the radius of the semicircle for CoS_2@FeS_2@NC is much smaller than that of the CoS_2@FeS_2 electrode, which indicates that the CoS_2@FeS_2@NC composite has better electrochemical reaction kinetics and faster charge transfer speed. Additionally, after 100 cycles at 1 A g^{-1}, the charge transfer resistance becomes smaller compared with before cycling, indicating that the conductivity and electrochemical activity of CoS_2@FeS_2@NC and CoS_2@

FeS_2 electrodes have been enhanced during cycling process. Compared with the previously reported TMCs-based anode materials for LIBs, the yolk-shell CoS_2@FeS_2@NC electrode exhibits the excellent lithium-ion property (Table S2 in the “Supplementary information”) [15, 35, 44, 51, 67–72]. The above results show that yolk-shell CoS_2@FeS_2@NC hollow microspheres own outstanding electrochemical performance and great application potential in lithium battery, which is consistent with our initial design.

Conclusion

In summary, yolk-shell CoS_2@FeS_2@NC hollow microspheres are fabricated and applied as advanced anode material for LIBs by a step-by-step strategy. This unique structure fully combines the advantages of NC coating and yolk-shell nanostructure, which markedly improve the specific capacity and cycling performance. Additionally, the FeS_2 nanoparticles well constrained by external NC can effectively reduce their aggregation and exfoliation, further enhancing the cycling stability of LIBs. As advanced anode materials for LIBs, the CoS_2@FeS_2@NC hollow microspheres can maintain a high capacity of 614 mAh g^{-1} at 1 A g^{-1} after 100 cycles. The results show that CoS_2@FeS_2@NC hybrid electrode owns superior electrochemical properties and great application potential in high-performance LIBs.

Supplementary Information The online version contains supplementary material available at https://doi.org/10.1007/s11581-022-04755-5.

Author contribution Dongxuan Liu: Conceptualization, experimental work. Weixing Min: Methodology, discussion. Ping Chen: Funding acquisition, writing—review and editing. Dongwei Xu: Revision the manuscript. Xinrong Cao: Discussion, software. Guanzhen Chen: Methodology. Ruiqi Wang: Software.

Funding This work was supported by the Liaoning Revitalization Talents Program (No. XLYC1802085), National Natural Science Foundation of China (No. 51873109), Fundamental Research Funds for the Central Universities (DUT20TD207), Dalian Science and Technology Innovation Fund Project (2019J11CY007), and Key Laboratory of Material Modification by Laser, Ion and Electron Beams of the Ministry of Education (No. KF2004).

Declarations

Competing interests The authors declare no competing interests.

References

1. Chiang YM (2010) Materials science. Building a better battery. Science 330:1485–1486
2. Dunn B, Kamath H, Tarascon JM (2011) Electrical energy storage for the grid: a battery of choices. Science 334:928–935
3. Goodenough JB, Park KS (2013) The Li-ion rechargeable battery: a perspective. J Am Chem Soc 135:1167–1176
4. Armand M, Tarascon J-M (2008) Building better batteries. Nature 451:652–657
5. He JR, Luo L, Chen YF, Manthiram A (2017) Yolk-Shelled C@Fe_3O_4 Nanoboxes as Efficient Sulfur Hosts for High-Performance Lithium-Sulfur Batteries. Adv Mater 29:1702707
6. He JR, Chen YF, Manthiram A (2019) Metal Sulfide-Decorated Carbon Sponge as a Highly Efficient Electrocatalyst and Absorbant for Polysulfide in High-Loading Li_2S Batteries. Adv Energy Mater 9:1900584
7. He JR, Hartmann G, Lee M, Hwang GS, Chen YF, Manthiram A (2019) Freestanding 1T MoS_2/graphene heterostructures as a highly efficient electrocatalyst for lithium polysulfides in Li-S batteries. Energy Environ Sci 12:344–350
8. He J, Chen YF, Manthiram A (2018) MOF-derived Cobalt Sulfide Grown on 3D Graphene Foam as an Efficient Sulfur Host for Long-Life Lithium-Sulfur Batteries. Iscience 4:36–43
9. Yang Z, Zhang J, Kintner-Meyer MC, Lu X, Choi D, Lemmon JP, Liu J (2011) Electrochemical energy storage for green grid. Chem Rev 111:3577–3613
10. Li X, Wang C (2013) Engineering nanostructured anodes via electrostatic spray deposition for high performance lithium ion battery application. J Mater Chem A 1:165–182
11. Zhao Y, Wang LP, Sougrati MT, Feng Z, Leconte Y, Fisher A, Srinivasan M, Xu Z (2017) A Review on Design Strategies for Carbon Based Metal Oxides and Sulfides Nanocomposites for High Performance Li and Na Ion Battery Anodes. Adv Energy Mater 7:1601424
12. Choi SH, Kang YC (2014) Synthesis for yolk-shell-structured metal sulfide powders with excellent electrochemical performances for lithium-ion batteries. Small 10:474–478
13. Wang F, Li F, Ma L, Zheng M (2019) Few-Layer MoS_2 Nanosheets Encapsulated in N-Doped Carbon Hollow Spheres as Long-Life Anode Materials for Lithium-Ion Batteries. Chemistry 25:14598–14603
14. Wu R, Wang DP, Rui X, Liu B, Zhou K, Law AW, Yan Q, Wei J, Chen Z (2015) In-situ formation of hollow hybrids composed of cobalt sulfides embedded within porous carbon polyhedra/carbon nanotubes for high-performance lithium-ion batteries. Adv Mater 27:3038–3044
15. Yang DD, Zhao M, Zhang RD, Zhang Y, Yang CC, Jiang Q (2020) NiS_2 nanoparticles anchored on open carbon nanohelmets as an advanced anode for lithium-ion batteries. Nanoscale Adv 2:512–519
16. Zhou Y, Yan D, Xu H, Feng J, Jiang X, Yue J, Yang J, Qian Y (2015) Hollow nanospheres of mesoporous Co_9S_8 as a high-capacity and long-life anode for advanced lithium ion batteries. Nano Energy 12:528–537
17. He JR, Bhargav A, Asl HY, Chen YF, Manthiram A (2020) 1T'-ReS_2 Nanosheets In Situ Grown on Carbon Nanotubes as a Highly Efficient Polysulfide Electrocatalyst for Stable Li-S Batteries. Adv Energy Mater 10:2001017
18. Qi F, Chen YF, Zheng BJ, He JR, Li Q, Wang XG, Lin J, Zhou JH, Yu B, Li PJ, Zhang WL (2017) Hierarchical architecture of ReS_2/rGO composites with enhanced electrochemical properties for lithium-ion batteries. Appl Surf Sci 413:123–128
19. Yu B, Chen YF, Wang ZG, Chen DJ, Wang XQ, Zhang WL, He JR, He WD (2020) 1T-MoS_2 nanotubes wrapped with N-doped graphene as highly-efficient absorbent and electrocatalyst for Li-S batteries. J Power Sources 447:227364
20. Chen B, Liu E, Cao T, He F, Shi C, He C, Ma L, Li Q, Li J, Zhao N (2017) Controllable graphene incorporation and defect engineering in MoS_2-TiO_2 based composites: Towards high-performance lithium-ion batteries anode materials. Nano Energy 33:247–256

21. Zhang Y, Lu F, Pan L, Xu Y, Yang Y, Bando Y, Golberg D, Yao J, Wang X (2018) Improved cycling stability of NiS_2 cathodes through designing a "kiwano" hollow structure. J Mater Chem A 6:11978–11984
22. Zhou J, Qin J, Zhao N, Shi C, Liu E-Z, He F, Li J, He C (2016) Salt-template-assisted synthesis of robust 3D honeycomb-like structured MoS_2 and its application as a lithium-ion battery anode. J Mater Chem A 4:8734–8741
23. Ran B, Cheng Z, Huawen H, Xinping W, Lei Z (2018) Metal–organic frameworks derived hollow NiS_2 spheres encased in graphene layers for enhanced sodium-ion storage. J Mater Chem A 6:14077–14082
24. Jiao Y, Mukhopadhyay A, Ma Y, Yang L, Hafez AM, Zhu H (2018) Ion Transport Nanotube Assembled with Vertically Aligned Metallic MoS_2 for High Rate Lithium-Ion Batteries. Adv Energy Mater 8:1702779
25. Tang W, Wang X, Zhong Y, Xie D, Zhang X, Xia X, Wu J, Gu C, Tu J (2018) Hierarchical MoS_2 /Carbon Composite Microspheres as Advanced Anodes for Lithium/Sodium-Ion Batteries. Chemistry 24:11220–11226
26. Li Z, Wu HB, Lou XW (2016) Rational designs and engineering of hollow micro-/nanostructures as sulfur hosts for advanced lithium–sulfur batteries. Energy Environ Sci 9:3061–3070
27. Yu XY, Yu L, Lou XW (2016) Metal Sulfide Hollow Nanostructures for Electrochemical Energy Storage. Adv Energy Mater 6:1501333
28. Fang Y, Luan D, Lou XW (2020) Recent Advances on Mixed Metal Sulfides for Advanced Sodium-Ion Batteries. Adv Mater 32:2002976
29. Geng P, Zheng S, Tang H, Zhu R, Zhang L, Cao S, Xue H, Pang H (2018) Transition Metal Sulfides Based on Graphene for Electrochemical Energy Storage. Adv Energy Mater 8:1703259
30. Hao Y, Chen C, Yang X, Xiao G, Zou B, Yang J, Wang C (2017) Studies on intrinsic phase-dependent electrochemical properties of MnS nanocrystals as anodes for lithium-ion batteries. J Power Sources 338:9–16
31. Pei J, Geng H, Ang EH, Zhang L, Cao X, Zheng J, Gu H (2018) Controlled synthesis of hollow $C@TiO_2@MoS_2$ hierarchical nanospheres for high-performance lithium-ion batteries. Nanoscale 10:17327–17334
32. Wang H, Lu S, Chen Y, Han L, Zhou J, Wu X, Qin W (2015) Graphene/Co_9S_8 nanocomposite paper as a binder-free and free-standing anode for lithium-ion batteries. J Mater Chem A 3:23677–23683
33. Wang H, Ma J, Liu S, Nie L, Chai Y, Yang X, Yuan R (2016) CoS/CNTs hybrid structure for improved performance lithium ion battery. J Alloys Compd 676:551–556
34. Xie H, Chen M, Wu L (2019) Hierarchical Nanostructured NiS/MoS_2/C Composite Hollow Spheres for High Performance Sodium-Ion Storage Performance. ACS Appl Mater Interfaces 11:41222–41228
35. Xue H, Jiao Q, Du J, Wang S, Feng C, Wu Q, Li H, Lu Q, Shi D, Zhao Y (2019) Hollow MoS_2/rGO composites as high-performance anode materials for lithium-ion batteries. Ionics 25:4659–4666
36. Qi F, He JR, Chen YF, Zheng BJ, Li Q, Wang XQ, Yu B, Lin J, Zhou JH, Li PJ, Zhang WL, Li YR (2017) Few-layered ReS_2 nanosheets grown on carbon nanotubes: A highly efficient anode for high-performance lithium-ion batteries. Chem Eng J 315:10–17
37. Shi L, Li D, Yao P, Yu J, Li C, Yang B, Zhu C, Xu J (2018) SnS_2 Nanosheets Coating on Nanohollow Cubic CoS_2/C for Ultralong Life and High Rate Capability Half/Full Sodium-Ion Batteries. Small 14:1802716
38. Pang WK, Zhou TF, Zhang CF, Yang JP, Chen ZX, Liu HK, Guo ZP (2014) Enhanced Sodium-Ion Battery Performance by Structural Phase Transition from Two-Dimensional Hexagonal-SnS_2 to Orthorhombic-SnS. ACS Nano 8:8323
39. Yu XY, Lou XW (2018) Mixed Metal Sulfides for Electrochemical Energy Storage and Conversion. Adv Energy Mater 8:1701592
40. Shen L, Yu L, Yu XY, Zhang X, Lou XW (2015) Self-templated formation of uniform $NiCo_2O_4$ hollow spheres with complex interior structures for lithium-ion batteries and supercapacitors. Angew Chem Int Ed Engl 54:1888–1892
41. Ma FX, Hu H, Wu HB, Xu CY, Xu Z, Zhen L, Lou XW (2015) Formation of Uniform Fe_3 O_4 Hollow Spheres Organized by Ultrathin Nanosheets and Their Excellent Lithium Storage Properties. Adv Mater 27:4097–4101
42. Shen L, Yu L, Wu HB, Yu XY, Zhang X, Lou XW (2015) Formation of nickel cobalt sulfide ball-in-ball hollow spheres with enhanced electrochemical pseudocapacitive properties. Nat Commun 6:6694
43. Ding X, Du C, Li J, Huang X (2019) FeS_2 microspheres wrapped by N-doped rGO from an Fe-based ionic liquid precursor for rechargeable lithium ion batteries. Sustainable Energy Fuels 3:701–708
44. Li Q, Yuan D, Wang X, Xue H, Liang F, Yin D, Wang L (2019) Facile synthesis of metal disulfides nanoparticles encapsulated by amorphous carbon composites as high-performance electrode materials for lithium storage. J Alloys Compd 773:97–104
45. Wang HC, Cui Z, Fan CY, Liu SY, Shi YH, Wu XL, Zhang JP (2018) 3 D Porous CoS_2 Hexadecahedron Derived from MOC toward Ultrafast and Long-Lifespan Lithium Storage. Chemistry 24:6798–6803
46. Maimaiti H, Awati A, Zhang D, Yisilamu G, Xu B (2018) Synthesis and photocatalytic CO_2 reduction performance of aminated coal-based carbon nanoparticles. RSC Adv 8:35989–35997
47. Ferrari AC, Robertson J (2000) Interpretation of Raman spectra of disordered and amorphous carbon. Phys Rev B 61:14095–14107
48. Chen GZ, Xu DW, Chen P, Guo X, Yu Q, Qiu HF (2021) Constructing and optimizing hollow bird-nest-patterned $C@Fe_3O_4$ composites as high-performance microwave absorbers. J Magn Magn Mater 532:167990
49. Wang HG, Wang YH, Li YH, Wan YC, Duan Q (2015) Exceptional electrochemical performance of nitrogen-doped porous carbon for lithium storage. Carbon 82:116–123
50. Chen X, Shi T, Zhong K, Wu G, Lu Y (2020) Capacitive behavior of MoS_2 decorated with $FeS_2@carbon$ nanospheres. Chem Eng J 379:122240
51. Lin Y, Qiu Z, Li D, Ullah S, Hai Y, Xin H, Liao W, Yang B, Fan H, Xu J, Zhu C (2018) $NiS_2@CoS_2$ nanocrystals encapsulated in N-doped carbon nanocubes for high performance lithium/sodium ion batteries. Energy Stor Mater 11:67–74
52. Guo D, Yuan H, Wang X, Zhu C, Chen Y (2020) Urchin-like Amorphous Nitrogen-Doped Carbon Nanotubes Encapsulated with Transition-Metal-Alloy@Graphene Core@Shell Nanoparticles for Microwave Energy Attenuation. ACS Appl Mater Interfaces 12:9628–9636
53. Xu X, Ran F, Fan Z, Cheng Z, Lv T, Shao L, Liu Y (2020) Bimetallic Metal-Organic Framework-Derived Pomegranate-like Nanoclusters Coupled with CoNi-Doped Graphene for Strong Wideband Microwave Absorption. ACS Appl Mater Interfaces 12:17870–17880
54. Zhang M, Xie H, Fan H, Zeng T, Yang W, Zheng W, Liang H, Liu Z (2020) Two-dimensional carbon-coated CoS_2 nanoplatelets issued from a novel $Co(OH)(OCH_3)$ precursor as anode materials for lithium ion batteries. Appl Surf Sci 516:146133
55. Xu QT, Xue HG, Guo SP (2018) FeS_2 walnut-like microspheres wrapped with rGO as anode material for high-capacity and long-cycle lithium-ion batteries. Electrochim Acta 292:1–9
56. Dong Y, Shi W, Lu P, Qin J, Zheng S, Zhang B, Bao X, Wu Z-S (2018) 2D holey cobalt sulfide nanosheets derived from

metal–organic frameworks for high-rate sodium ion batteries with superior cyclability. J Mater Chem A 6:14324–14329
57. Xia H, Li K, Guo Y, Guo J, Xu Q, Zhang J (2018) CoS_2 nanodots trapped within graphitic structured N-doped carbon spheres with efficient performances for lithium storage. J Mater Chem A 6:7148–7154
58. Wang J, Fang J, Zhao H, Zhang Z, Li Z (2021) Raspberry-like hierarchical structure FeS_2 decorated by dual-carbon framework as high-performance cathode for rechargeable lithium batteries. Carbon 171:171–178
59. Wu H, Chan G, Choi JW, Ryu I, Yao Y, McDowell MT, Lee SW, Jackson A, Yang Y, Hu L, Cui Y (2012) Stable cycling of double-walled silicon nanotube battery anodes through solid-electrolyte interphase control. Nat Nanotechnol 7:310–315
60. Wang X, Qiao L, Sun X, Li X, Hu D, Zhang Q, He D (2013) Mesoporous NiO nanosheet networks as high performance anodes for Li ion batteries. J Mater Chem A 1:4173–4176
61. Li J, Xiong S, Liu Y, Ju Z, Qian Y (2013) High electrochemical performance of monodisperse $NiCo_2O_4$ mesoporous microspheres as an anode material for Li-ion batteries. ACS Appl Mater Interfaces 5:981–988
62. Liu Y, Zhang L, Zhao Y, Shen T, Yan X, Yu C, Wang H, Zeng H (2019) Novel plasma-engineered MoS_2 nanosheets for superior lithium-ion batteries. J Alloys Compd 787:996–1003
63. Liu Y, Zhang L, Wang H, Yu C, Yan X, Liu Q, Xu B, Wang LM (2018) Synthesis of severe lattice distorted MoS_2 coupled with hetero-bonds as anode for superior lithium-ion batteries. Electrochim Acta 262:162–172
64. Li H, Su Y, Sun W, Wang Y (2016) Carbon Nanotubes Rooted in Porous Ternary Metal Sulfide@N/S-Doped Carbon Dodecahedron: Bimetal-Organic-Frameworks Derivation and Electrochemical Application for High-Capacity and Long-Life Lithium-Ion Batteries. Adv Funct Mater 26:8345–8353
65. Li Z, Ottmann A, Zhang T, Sun Q, Meyer HP, Vaynzof Y, Xiang J, Klingeler R (2017) Preparation of hierarchical C@MoS_2@C sandwiched hollow spheres for lithium ion batteries. J Mater Chem A 5:3987–3994
66. Zhang L, Huang Y, Zhang Y, Gu H, Fan W, Liu T (2016) Flexible Electrospun Carbon Nanofiber@NiS Core/Sheath Hybrid Membranes as Binder-Free Anodes for Highly Reversible Lithium Storage. Adv Mater Interfaces 3:1500467
67. Xu X, Ying HJ, Zhang SL, Meng Z, Yan XF, Han WQ (2020) Biomass derived 3D interconnected porous carbon encapsulated nano-FeS_2 for high-performance lithium-ion batteries. ACS Appl Energy Mater 3:5589–5596
68. Qian X, Zhu G, Wang K, Zhang F, Liang K, Luo W, Yang J (2020) Bowl-like mesoporous polymer-induced interface growth of molybdenum disulfide for stable lithium storage. Chem Eng J 381:122651
69. Wan Z, Shao J, Yun J, Zheng H, Gao T, Shen M, Qu Q, Zheng H (2014) Core-shell structure of hierarchical quasi-hollow MoS_2 microspheres encapsulated porous carbon as stable anode for Li-ion batteries. Small 10:4975–4981
70. Wang Q, Zou R, Xia W, Ma J, Qiu B, Mahmood A, Zhao R, Yang Y, Xia D, Xu Q (2015) Facile Synthesis of Ultrasmall CoS_2 Nanoparticles within Thin N-Doped Porous Carbon Shell for High Performance Lithium-Ion Batteries. Small 11:2511–2517
71. Xue H, Yue S, Wang J, Zhao Y, Li Q, Yin M, Wang S, Feng C, Wu Q, Li H, Shi D, Jiao Q (2019) MoS_2 microsphere@ N-doped carbon composites as high performance anode materials for lithium-ion batteries. J Electroanal Chem 840:230–236
72. Zhao J, Hu Z, Sun D, Jia H, Liu X (2019) MOF-Derived FeS/C nanosheets for high performance lithium ion batteries. Nanomaterials (Basel, Switzerland) 9:492